



A Bearingless Switched-Reluctance Motor for High Specific Power Applications

Benjamin B. Choi
Glenn Research Center, Cleveland, Ohio

Mark Siebert
University of Toledo, Toledo, Ohio

NASA STI Program . . . in Profile

Since its founding, NASA has been dedicated to the advancement of aeronautics and space science. The NASA Scientific and Technical Information (STI) program plays a key part in helping NASA maintain this important role.

The NASA STI Program operates under the auspices of the Agency Chief Information Officer. It collects, organizes, provides for archiving, and disseminates NASA's STI. The NASA STI program provides access to the NASA Aeronautics and Space Database and its public interface, the NASA Technical Reports Server, thus providing one of the largest collections of aeronautical and space science STI in the world. Results are published in both non-NASA channels and by NASA in the NASA STI Report Series, which includes the following report types:

- **TECHNICAL PUBLICATION.** Reports of completed research or a major significant phase of research that present the results of NASA programs and include extensive data or theoretical analysis. Includes compilations of significant scientific and technical data and information deemed to be of continuing reference value. NASA counterpart of peer-reviewed formal professional papers but has less stringent limitations on manuscript length and extent of graphic presentations.
- **TECHNICAL MEMORANDUM.** Scientific and technical findings that are preliminary or of specialized interest, e.g., quick release reports, working papers, and bibliographies that contain minimal annotation. Does not contain extensive analysis.
- **CONTRACTOR REPORT.** Scientific and technical findings by NASA-sponsored contractors and grantees.

- **CONFERENCE PUBLICATION.** Collected papers from scientific and technical conferences, symposia, seminars, or other meetings sponsored or cosponsored by NASA.
- **SPECIAL PUBLICATION.** Scientific, technical, or historical information from NASA programs, projects, and missions, often concerned with subjects having substantial public interest.
- **TECHNICAL TRANSLATION.** English-language translations of foreign scientific and technical material pertinent to NASA's mission.

Specialized services also include creating custom thesauri, building customized databases, organizing and publishing research results.

For more information about the NASA STI program, see the following:

- Access the NASA STI program home page at <http://www.sti.nasa.gov>
- E-mail your question via the Internet to help@sti.nasa.gov
- Fax your question to the NASA STI Help Desk at 301-621-0134
- Telephone the NASA STI Help Desk at 301-621-0390
- Write to:
NASA STI Help Desk
NASA Center for AeroSpace Information
7115 Standard Drive
Hanover, MD 21076-1320



A Bearingless Switched-Reluctance Motor for High Specific Power Applications

Benjamin B. Choi
Glenn Research Center, Cleveland, Ohio

Mark Siebert
University of Toledo, Toledo, Ohio

Prepared for the
42nd Joint Propulsion Conference and Exhibit
cosponsored by the AIAA, ASME, SAE, and ASEE
Sacramento, California, July 9–12, 2006

National Aeronautics and
Space Administration

Glenn Research Center
Cleveland, Ohio 44135

Acknowledgments

The authors would like to thank Dr. Gerald Brown for his technical guidance throughout this work and Ben Ebihara and Carl Buccieri for their significant contribution to the motor design and fabrication. We would also like to thank James Walker, NASA Glenn project manager for the Noncombustion Based Propulsion Project, for financial support

This work was sponsored by the Fundamental Aeronautics Program
at the NASA Glenn Research Center.

Level of Review: This material has been technically reviewed by technical management.

Available from

NASA Center for Aerospace Information
7115 Standard Drive
Hanover, MD 21076-1320

National Technical Information Service
5285 Port Royal Road
Springfield, VA 22161

Available electronically at <http://gltrs.grc.nasa.gov>

A Bearingless Switched-Reluctance Motor for High Specific Power Applications

Benjamin B. Choi
National Aeronautics and Space Administration
Glenn Research Center
Cleveland, Ohio 44135

Mark Siebert
University of Toledo
Toledo, Ohio 43606

A 12-8 switched-reluctance motor (ref. 1) (SRM) is studied in bearingless (or self-levitated) operation with coil currents limited to the linear region to avoid magnetic saturation. The required motoring and levitating currents are summed and go into a single motor coil per pole to obtain the highest power output of the motor by having more space for motor coil winding. Two controllers are investigated for the bearingless SRM operation. First, a model-based controller using the radial force in reference 2, which is adjusted by a factor derived from finite element analysis, is presented. Then a simple and practical observation-based controller using a PD (proportional-derivative) control algorithm is presented. Both controllers were experimentally demonstrated to 6500 rpm. This paper reports the initial efforts toward eventual self levitation of a SRM operating into strong magnetic core saturation at liquid nitrogen temperature.

Nomenclature

N	number of turns of the motor winding
$P_{a1} \sim P_{a4}$	permeances of the air gap at phase A winding poles
P	sum of the permeances $P_{a1} \sim P_{a4}$
$\phi_{a1} \sim \phi_{a4}$	magnetic fluxes of each tooth
i_{ma}	motor winding current at phase A
i_{a1}	levitation current on the a_1 axis at phase A
i_{a2}	levitation current on the a_2 axis at phase A
L_{ma}	self-inductance of magnetic flux produced by i_{a1}
L_{sa1}, L_{sa2}	self-inductance of magnetic flux produced by i_{a1}, i_{a2}
$M_{(ma,sa1)}$	mutual inductance between magnetic flux produced by i_{ma} and i_{a1}
$M_{(ma,sa2)}$	mutual inductance between magnetic flux produced by i_{ma} and i_{a2}
$M_{(sa1,sa2)}$	mutual inductance between magnetic flux produced by i_{a1} and i_{a2}
h	stack length of lamination
c	constant
r	radius of rotor poles
θ_a	rotor rotational position in phase A
l_g	air-gap length
μ_o	permeability in the air
α	rotor displacement in the $sa1$ axis
β	rotor displacement in the $sa2$ axis
θ_m	firing angle of motoring and levitating currents
θ_w	pulse signal width of motoring and levitating currents
d	derivative gain
k	actual magnetic bearing net stiffness
k_s	negative magnetic bearing stiffness
ki	current stiffness

1. Introduction

The NASA Glenn Research Center has been developing high-power-density motors (refs. 1 and 4) for possible use for pollution-free flight. One suggested method of achieving that goal is a hydrogen-fueled aircraft that could use turbogenerators to develop electric power for motors that rotate the aircraft's propulsive fans or propellers. Hydrogen fuel would likely be carried as a liquid, which could provide essentially free refrigeration to cool electric motor windings before being used as fuel. Recently, we demonstrated improved performance of a switched-reluctance motor (SRM) (fig. 1), stemming mainly from cryogenic operation and coil design, surpassing (we believe) previous specific torque and specific tangential force records for the motor type. Furthermore, we anticipate more motor-specific power by upgrading electric power conditioning and coil windings.

However, cryogenic operation at higher rotational speeds markedly shortens the life of mechanical rolling element bearings. Even without cryogenics, conventional bearing life may be limited at the high speeds possible with SRMs. Thus, to demonstrate the practical feasibility of using this high-power-density motor, a noncontact rotor-bearing system is a crucial technology. During the last decade, a variety of bearingless motors have been introduced, including permanent magnet (refs. 5 and 6), induction (refs. 7 and 8), and reluctance types (refs. 2, 3, 9, and 10). These motors have their own characteristics and applications. Among them, the SRM is a favored candidate for future airborne systems because it has inherent fault-tolerance and rotor robustness and reliability at high rotational speeds (no coil windings on the rotor).

Since the SRM has doubly salient structure, it is not possible to obtain an exact analytical expression for its plant model. Numerous authors have addressed this problem with solutions using Maxwell stress tensor, finite element method (FEM), flux tube, and so forth. Takemoto et al. (ref. 10) in 2001 published a significant technical accomplishment on a successful controller demonstration of a 12-8 (12 poles in the stator and 8 poles in the rotor) bearingless SRM up to 2500 rpm. They developed a much simplified mathematical expression of the radial bearing force equation based on results of FEM analysis to express fringing fluxes and neglecting magnetic saturation. However, they added a separate magnetic bearing coil winding to each stator pole motor winding for the rotor levitation (a total of 2 coils per stator pole), resulting in additional power amplifiers and associated electrical subsystem for the extra 12 magnetic bearing coils. Furthermore, their controller is still a very complicated mathematical-model-based controller, which requires considerable effort for controller design and implementation.

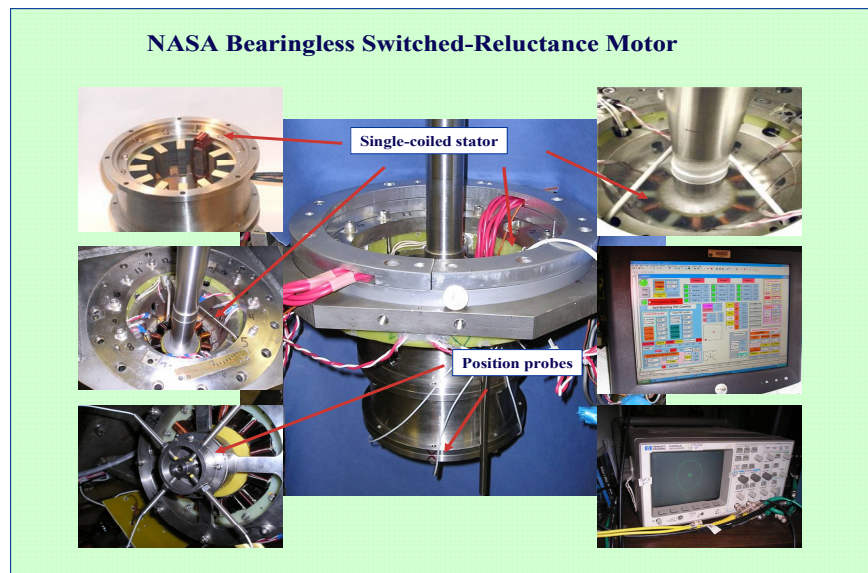


Figure 1.— NASA bearingless switched-reluctance motor.

In this paper, a simple and practical PD (proportional-derivative) controller is presented for the bearingless (or self-levitated) operation of our SRM operating at room temperature with the coil currents limited to the linear region to avoid magnetic saturation. Compared to the previous work done by Takemoto et al. (ref. 2) and Shuang et al. (ref. 3), our work has two features in hardware and software. First, the motor does not have separate coils for motor action and magnetic bearing action, but only motor coils as in a conventional motor configuration. We favor the single-coil approach because it is more conducive to higher specific power. The single coil idea was originally proposed by Higuchi et al. (ref. 11) in 1989 and Preston et al. (ref. 12) applied it more specifically to the 12-8 switched-reluctance machine in 1995. However, to our knowledge, they did not publish an account of successful operation or describe the nature of their controller. Takemoto also considered the single winding concept, but decided to add separate levitation coils to the stator pole to counter amplifier problems at higher rotational speed. Second, as opposed to researchers who required a mathematical plant model in their controller, we have avoided mathematical complexity by using an observation-based controller, which can be implemented in real-time at much higher rotor speed. These features are important factors for aerospace application of this motor because it improves power output by having more space for motor coil winding, resulting in lower system weight and improved system reliability.

First we describe a model-based controller, mainly following the procedure developed by Takemoto et al., but modifying it somewhat based on some three-dimensional finite element results. The resulting controller was successfully demonstrated experimentally. Then we demonstrated a much simpler observation-based PD controller for levitation, which does not require any mathematical plant models and is advantageous at high motor speed due to a less computation-intensive method.

2. Motor Configuration

As shown in figure 1, the motor is mounted with a vertical axis to simplify submersion in LN₂. A dynamometer is mounted on the top with a flexible coupling to control the rotor speed up to 20 000 rpm. The stator O.D. is 7.25 in. (18.4 cm); the rotor O.D. is 3.96 in. (10.1 cm) and the axial length of the lamination stack is 1.97 in. (5.08 cm). The radial air gap is 0.02 in. (0.051 cm). The stator-pole arc, the stator-pole-gap arc, and the rotor-pole arc are all equal. The laminations are 0.006 in. (0.152 mm) thick and are made of Hiperco 50 HS. When operated on conventional rolling element bearings, the 18-lb motor developed a specific torque of 1.8 ft-lb/lb and achieved the specific power of 3.5 Hp/lb-EM. We anticipate more specific power by power conditioning improvement and further upgrades.

Figure 2 shows only the phase A stator winding configuration of the 12-8 SRM. The arc angle of the rotor and stator teeth is 15° (mechanical angle). The motor winding on each stator pole is connected to an independent power amplifier, which has a ± 170 V_{max} and ± 15 A rms continuous current. Since there are no separate levitation coils, the required motoring and levitating currents for each pole are mathematically summed and applied as a single current to the motor pole winding. The phase B windings are shifted clockwise by 15° relative to the phase A; the phase C windings by 15° relative to the phase B. Square-wave excitation current is applied to energize each phase and the interval is defined by the firing angle θ_m and signal pulse width θ_w (15° default value). The motoring torques and levitation forces are generated by these three phases for every 15°, between the start of overlap and aligned positions. The rotor angular position, θ , is defined as $\theta=0$ at the aligned position of the phase A.

In α -direction from figure 2, the motor main winding generates a biasing flux, whose flux density is increased at one air gap and decreased at the other air gap by flux density generated by the two-pole radial force current i_{a1} direction, and thus this superimposed imbalance of flux density results in the radial force F_α acting on the rotor in the α -direction. Similarly, a radial force in the β -direction can be produced by the two-pole radial force current i_{a2} . Thus, radial force can be generated in any desired direction. This principle can be applied to phases B and C.

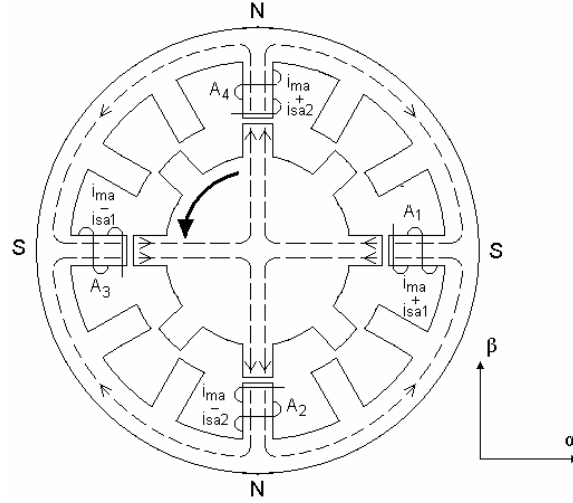


Figure 2.—Phase A motor winding configuration and levitation current polarity of the motor.

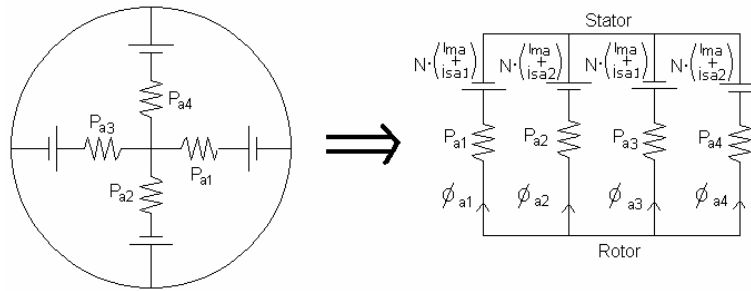


Figure 3.—A magnetic equivalent circuit of phase A.

3. Radial Forces and Model-Based Controller Implementation

In this section, we compare the radial force predictions of Takemoto et al., Shuang et al., and our own three-dimensional finite element calculation. Based on the results we implemented an angle-dependent correction to the Takemoto et al. controller for our initial experimental trials.

3.1 Derivation of Inductance

Figure 3 shows a magnetic equivalent circuit for phase A only. Voltage sources represent magnetomotive forces (MMFs) of the four-pole motor currents and the two-pole levitation currents. Permeances of the air gaps are shown as $P_{a1} \sim P_{a4}$ and are expressed as equivalent resistances. Since Takemoto et al. derived well the flux-linkage formula (ref. 2), we plugged our configuration into their formula and obtained.

$$\begin{bmatrix} \psi_{ma} \\ \psi_{sa1} \\ \psi_{sa2} \end{bmatrix} = \begin{bmatrix} L_{ma} & M_{(ma,sa1)} & M_{(ma,sa2)} \\ M_{(ma,sa1)} & L_{sa1} & M_{(sa1,sa2)} \\ M_{(ma,sa2)} & M_{(sa2,sa1)} & L_{sa2} \end{bmatrix} \begin{bmatrix} i_{ma} \\ i_{sa1} \\ i_{sa2} \end{bmatrix} \quad (1)$$

where the self-inductance and mutual inductance are

$$\begin{aligned}
L_{ma} &= \frac{4N^2(P_{a1} + P_{a3})(P_{a2} + P_{a4})}{P} \\
L_{sa1} &= \frac{N^2\{P_{a1}(P_{a2} + 2P_{a3} + P_{a4}) + P_{a3}(2P_{a1} + P_{a2} + P_{a4})\}}{P} \\
L_{sa2} &= \frac{N^2\{P_{a2}(P_{a1} + P_{a3} + 2P_{a4}) + P_{a4}(P_{a1} + 2P_{a2} + P_{a3})\}}{P} \\
M_{(ma,sa1)} &= + \frac{2N^2(P_{a1} - P_{a3})(P_{a2} + P_{a4})}{P} \\
M_{(ma,sa2)} &= - \frac{2N^2(P_{a1} + P_{a3})(P_{a2} - P_{a4})}{P} \\
M_{(sa1,sa2)} &= - \frac{N^2(P_{a1} - P_{a3})(P_{a2} - P_{a4})}{P}
\end{aligned} \tag{2}$$

In case of stably controlled rotor position (i.e., $\alpha = \beta = 0$), the permeance for each air gap will be the same and the mutual inductance in equation (2) will be cancelled out and thus it is easy to control F_α and F_β independently.

3.2 Radial Force Equation

The stored magnetic energy, W_a , is given by one-half of the inductance of the coil times the square of the current. Thus, the radial forces F_α and F_β can be derived from the derivatives of the stored magnetic energy with respect to the displacements α and β , respectively. A simplified mathematical expression of the radial force was proposed in reference 2 and plugging our motor's configuration into the formula gives

$$F_\alpha = \frac{\partial W_a}{\partial \alpha} = N^2 \left[\frac{\mu_o hr(\pi - 12\theta_a)}{6l_o^2} + \frac{32\mu_o hrc\theta_a}{\pi(4rc\theta_a(l_o + \alpha) + \pi l_o^2)} \right] i_{ma} i_{sa1} \tag{3}$$

$$F_\beta = \frac{\partial W_a}{\partial \beta} = N^2 \left[\frac{\mu_o hr(\pi - 12\theta_a)}{6l_o^2} + \frac{32\mu_o hrc\theta_a}{\pi(4rc\theta_a(l_o + \beta) + \pi l_o^2)} \right] i_{ma} i_{sa2} \tag{4}$$

The first term of the force expression is from the permeances between rotor and poles and the second term is from the fringing flux path, respectively. In reference 14, a new force equation that takes into account the cross coupling between the x- and y-axes radial forces was proposed. However, the change in the radial force prediction from the new coupled formula showed little difference, which had a negligible effect as shown by simulation using MatLab/Symbolic software. Thus, for the simplicity of radial force expression, equations (3) and (4) are used in this paper.

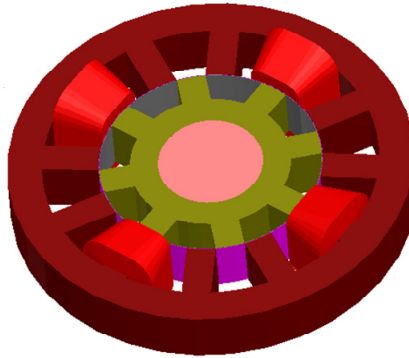


Figure 4.—A Maxwell three-dimensional model of the motor for FEM analysis.

TABLE I.— MAIN DIMENSIONS OF THE MOTOR

Stack length, h	2 in.
Average air-gap length, l_g	0.02 in.
Constant, c	1.49
Rotor pole radius, r	1.98 in.
Number of turns of main winding, N	80
Motoring current, i_m	8 amps
Levitation current in x-axis, i_{sa1}	2 amps
Levitation current in y-axis, i_{sa2}	2 amps

In 2002, Shuang et al. (ref. 3) also proposed new formulae for radial forces based on Fourier analysis of the permeance. In order to investigate the accuracy of the various radial force equations, we created a three-dimensional Maxwell model (fig. 4) for the finite element analysis of inductance and radial force and compared our FEM results with Takemoto's and Shuang's results. Table I shows a summary of main dimensions of the motor and parameters for the radial force calculation.

Figure 5 shows the radial forces calculated by using Takemoto's formula in equations (3) and (4), Shuang's new formula in reference 3, and a Maxwell three-dimensional FEM analysis from fully aligned to unaligned rotor positions. It is observed that Shuang's and Takemoto's results agreed well, except from 0° to about 2.5° (0.044 radians) of the rotor positional angles from fully aligned position. Overall Shuang's radial force formula looked more realistic than Takemoto's formula. However, Takemoto's mathematical equation was selected to implement the first bearingless controller because it is easier to invert for calculating the levitation control current needed to produce a given radial force. Here, we assume that the FEM represents the real motor model. The difference between Takemoto's radial force prediction and the FEM result from the fully aligned position to the end of overlap position was utilized in our controller to minimize the required control current error. For the instantaneous rotor angle for each phase, the levitating current is increased by the ratio of Takemoto's force to the FEM force shown in figure 5, from 0° to 15° (0.262 radians) of the rotor positional angles.

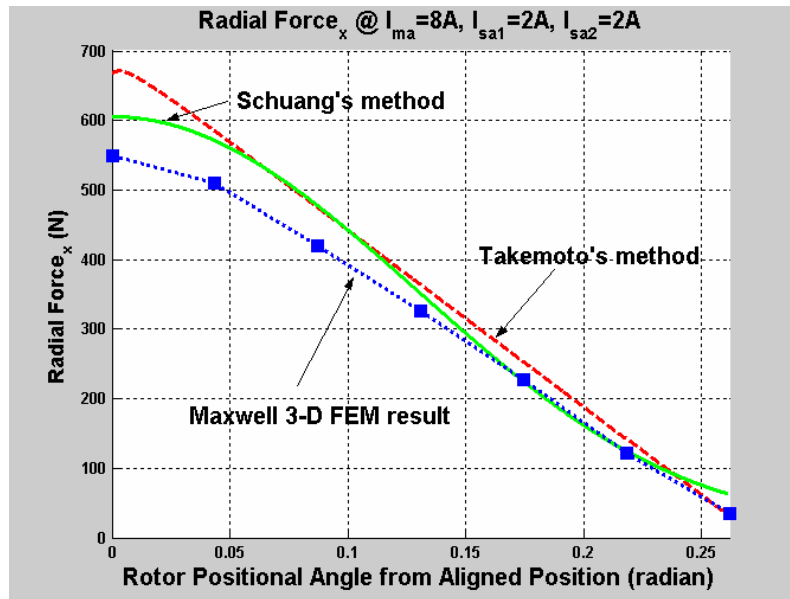


Figure 5.—Static radial force prediction.

3.3 Model-Based Controller Implementation

A control algorithm was implemented by inverting the radial force equations in equations (3) and (4). For given radial force and motoring current, the required levitation current is calculated and summed with the motoring current. The superimposed currents go to the single motor coil through a pulse-width modulation (PWM) power amplifier. MatLab/Simulink software was used for a closed-loop simulation of motoring and a dSPACE system was used for the real-time motor control system.

Figure 6 shows a simplified block diagram of the control system where the rotor radial position is controlled with a negative feedback loop. At the beginning of motor operation, an auto kickstart is implemented based on a simple algorithm. First, a ramp-up signal is generated slowly and stays for a while to obtain a fully aligned rotor position and then the motor current for the next phase is generated for a certain period. Four position probes (see fig. 1) mounted near the bottom of the motor shaft sense the shaft radial position and those signals are fed back to the controller blocks for magnetic bearing action. Also an eight-per-rev signal is fed back to the front part of the controller to calculate the rotor angular position and speed and to identify the phase. Those inputs are necessary to calculate levitation current for each phase. For phases B and C, which are shifted by 15° and 30° relative to phase A, respectively, a transformation matrix is used to calculate the levitation currents for those two phases. There is a software speed control switch to select one of three choices for the motor speed control. The first is to use a dynamometer attached on the top of the motor, which can control the motor up to 20 000 rpm. The second is an open-loop control in which we choose the firing angle, pulse width, and the motoring current to manipulate the amount of positive and negative torques (see fig. 7). The last option is a closed-loop speed control (refs. 13 and 14), which has been successfully implemented.

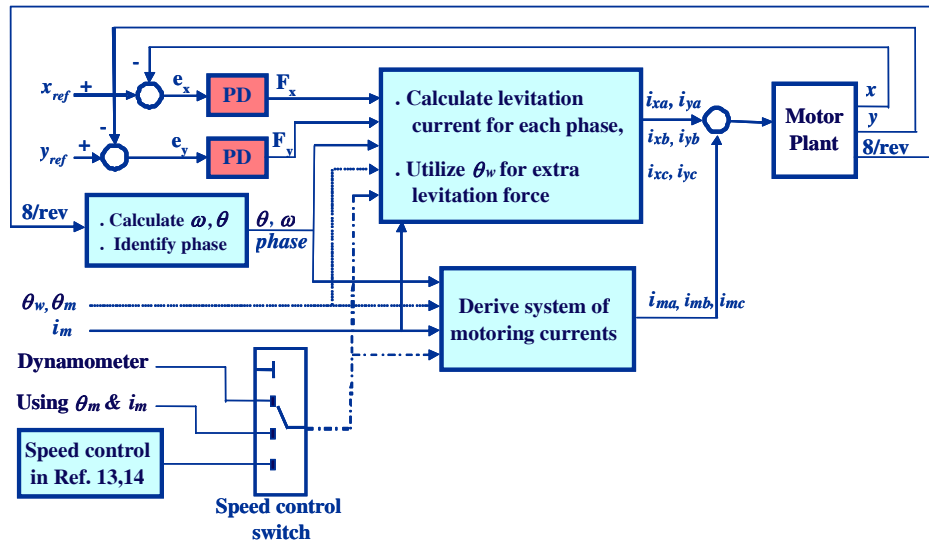


Figure 6.—Simplified block diagram of control system.

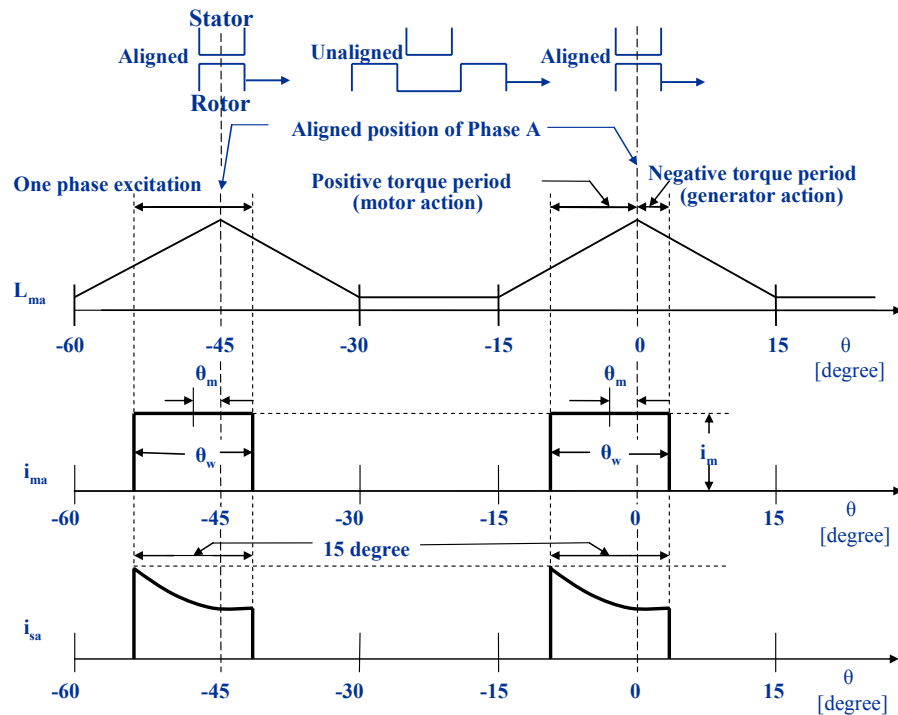


Figure 7.—Phase A energizing for motoring and levitation.

We ran the motor from 0 rpm up to 6500 rpm (maximum allowable speed at that time) with small rotor orbits. Figures 8 through 10 show the experimental data of the rotor orbit (shown within the backup bearing clearance circle), the command signal from the controller, and the actual current applied to PWM amplifier for each phase. As shown in the figures, the rotor is quite stable and maintains within less than 10 percent of the backup bearing clearance. The required levitation current is less than 10 percent of the motoring current.

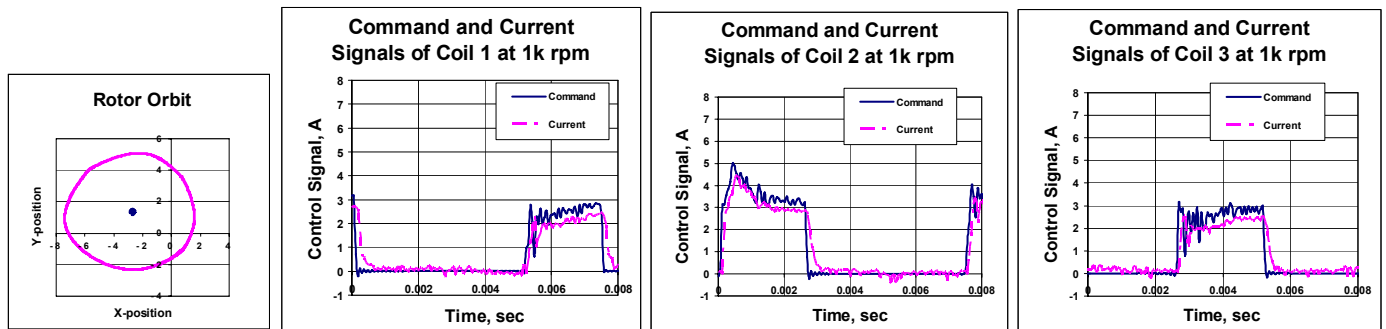


Figure 8.—Rotor orbit within backup bearing clearance circle, command signals and actual currents at 1k rpm.

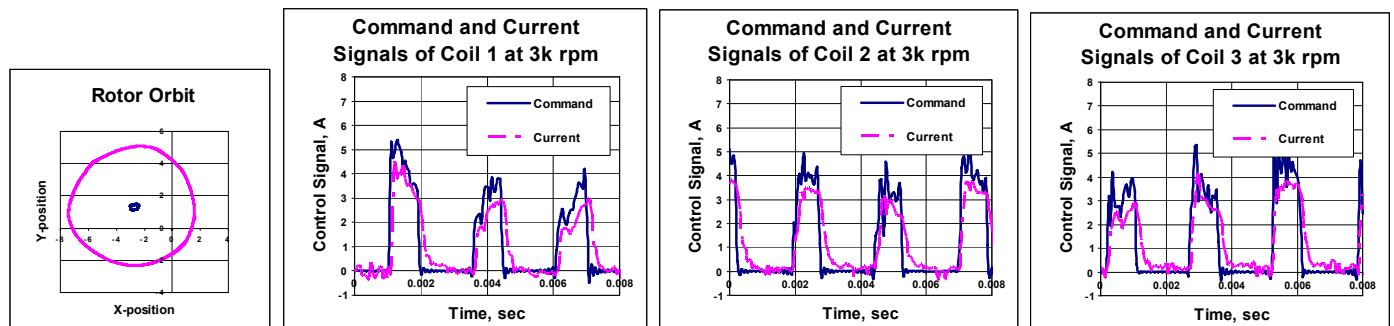


Figure 9.—Rotor orbit within backup bearing clearance circle, command signals and actual currents at 3k rpm.

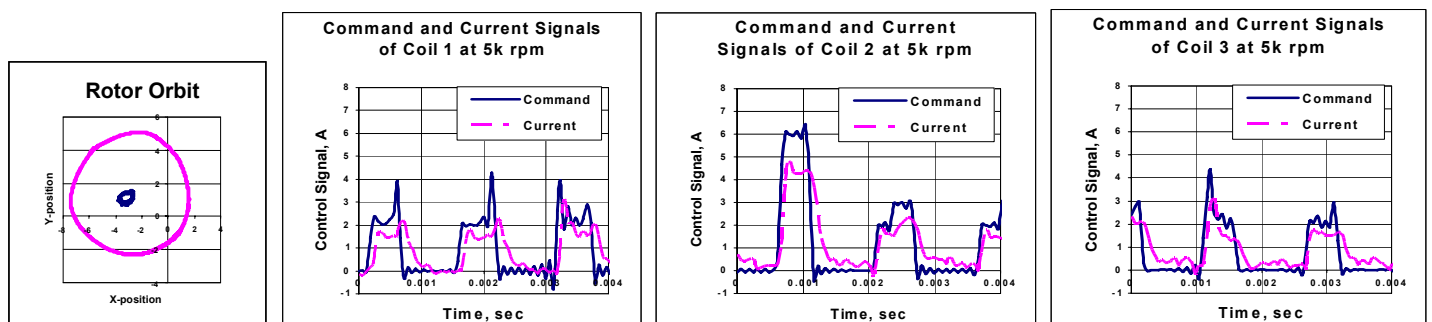


Figure 10.—Rotor orbit within backup bearing clearance circle, command signals and actual currents at 5k rpm.

4. A Simple PD Controller

In the previous section, we showed a model-based controller, which required a somewhat complicated derivation of a mathematical expression of radial force. In this section, we present an observation-based controller using a PD control scheme, which does not require a plant model for controller design. Its control law is

$$i(x, \dot{x}) = -\frac{(k + k_s) \cdot x + d \cdot \dot{x}}{k_i} \quad (5)$$

with a proportional gain $P = (k + k_s) / k_i$ and a derivative gain $D = d / k_i$. The proportional gain includes a term to offset the negative bearing stiffness k_s and one to produce the actual bearing net stiffness k . The derivative component controls the damping of the rotor radial positions. The D term was digitally realized as (current position—previous position)/sample time. The only constraint is that the levitation current cannot be greater than the motoring current to avoid the polarity change of stator pole for each phase. A much simplified controller block diagram is thereby obtained by eliminating the calculation block (see fig. 6) for levitation currents. The rest of the controller features are the same as described in section 4.3.

4.1 Stability Map

As the first steps in operating the motor, we determine which combinations of proportional and derivative gains produce stable operation. Beginning at low speed, a stability map is obtained experimentally at each successive speed by changing one gain with the other gain fixed until the rotor orbit hits the predefined orbit limit. These gain sets show stability surface under which stable operation of the system is achieved at the entire operating range. While testing the new controller parameters, the middle range gain set is selected and plugged into the controller as a “safe” gain set, which is triggered to protect the bearing system at higher speeds when the rotor orbit exceeds the predefined orbit size. Figure 11 shows a stability map of the proportional and derivative controller safe gains. In each case the stable area lies between the two plotted curves.

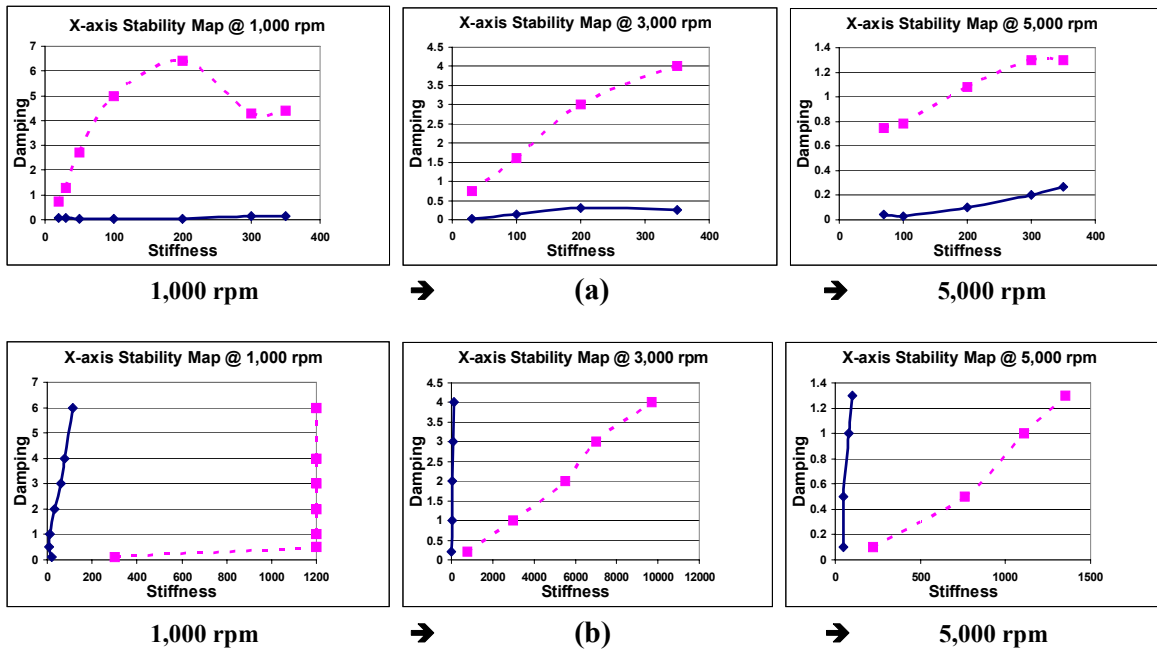


Figure 11. An x-axis stability map. A y-axis stability map obtained similarly.

4.2 Fault Tolerance

A SRM has inherent fault-tolerant motoring operation. However, to investigate the self-levitated motoring operation, a quasi-fault-tolerant feature by providing zero currents to certain coils is added to the controller cockpit window. At low levitation currents, a small offset from the reference position occurs where a coil current is suddenly switched off. When an integral feedback scheme is implemented with the existing PD controller, any deviation of the position is integrated over time slowly and added to the feedback until the error signal e becomes zero. We tested a variety of fault-tolerant bearingless motor operations and achieved a fault-tolerant operation using only 6 certain coils (not arbitrarily selected) out of 12 coils. A more detailed discussion is beyond this paper's scope. In addition, there is a switch to utilize an integrator at the control force output to find the magnetic force center to minimize the control effort.

4.3 Controller Cockpit Window

Figure 12 shows the MatLab/Simulink model for the closed-loop simulation for the real-time motor controller. A user-friendly controller cockpit window for the dSPACE control system (fig. 13) allows modification of control parameters and aforementioned features such as automatic kickstart, speed control method, motor current, firing angle, pulse width, and stiffness and damping gains for the PD controller, fault tolerance, and so forth. In addition to an external comprehensive data collecting system, a simple data acquisition capability is added to the control cockpit window to monitor the system performance.

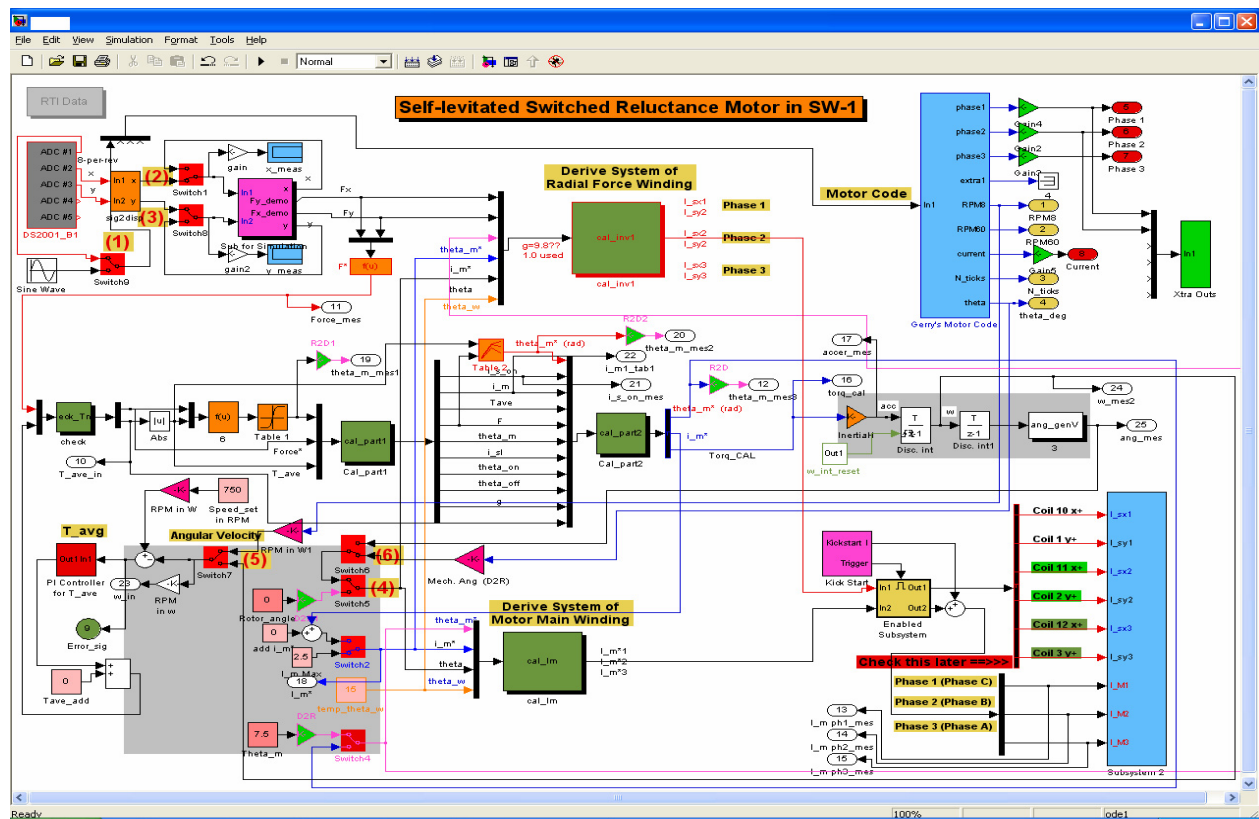


Figure 12.—MatLab/Simulink closed-loop system model that represents the bearingless motor control system.

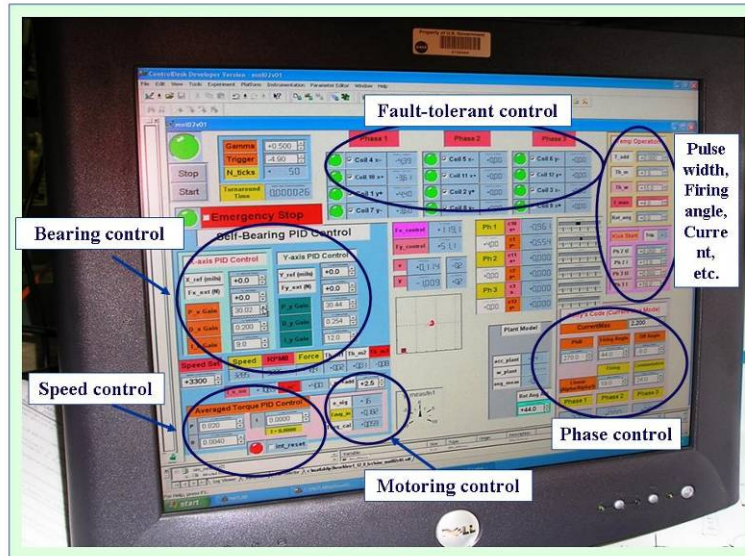


Figure 13.—Controller cockpit window for the dSPACE control system.

4.4 Controller Results

By using the simple PD controller, we ran the motor from 0 rpm up to 6500 rpm. The rotor orbits were small and solid over the entire operating range, but some high-frequency noise remained in the control current. The rotor orbit around 4600 rpm was somewhat shaky with relatively larger vibration amplitude and control current at the time of data collection. Notice that even the largest rotor orbits are within less than 10 percent of backup bearing clearance and the required levitation current is less than 10 percent of the motoring current. Figures 14 through 16 show the experimental data of the rotor orbit, shown within the backup bearing clearance circle, command signal from the controller, and the actual current applied to PWM amplifier for each phase.

Compared to the model-based controller's performance shown in figures 8 through 10, the PD controller performance is similar in terms of the rotor orbit and control current amplitude. A more sophisticated comparison in terms of bearing load capacity, torque, and power will be presented in the next publication.

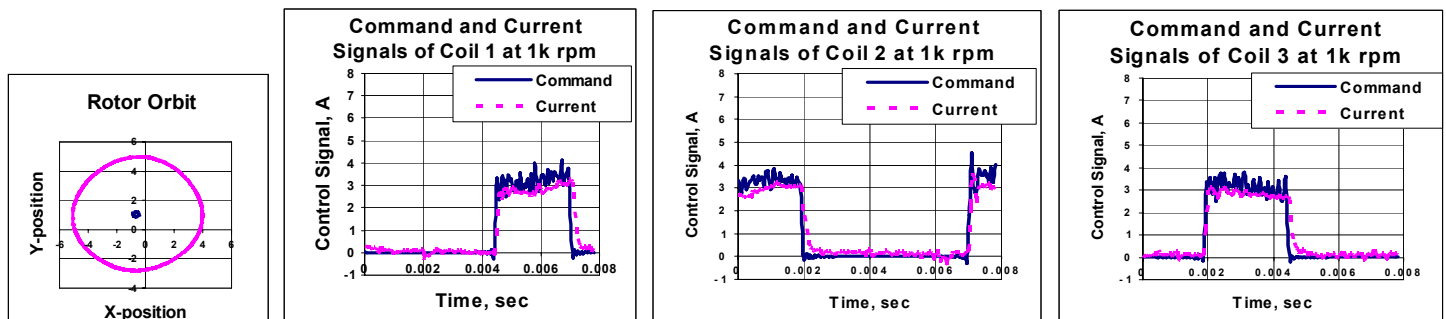


Figure 14.—Rotor orbit within backup bearing clearance circle and command and actual current signals at 1k rpm.

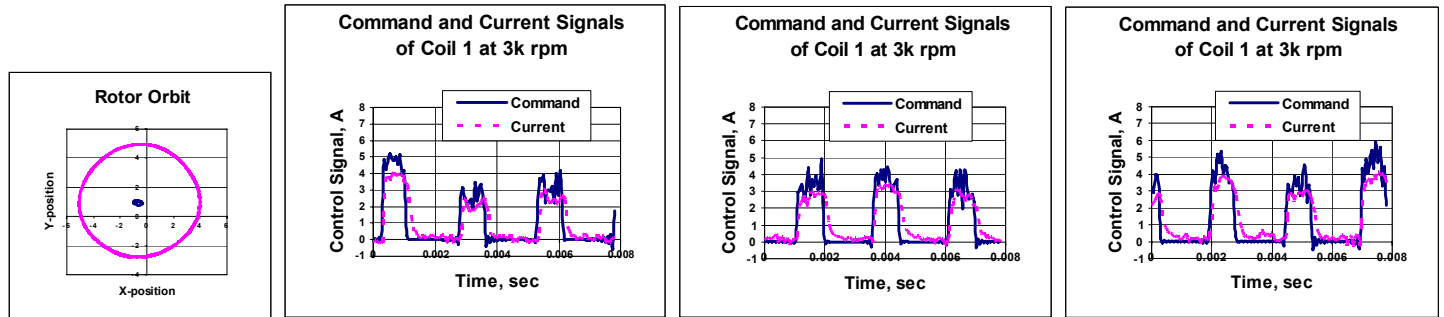


Figure 15.—Rotor orbit within backup bearing clearance circle and command and actual current signals at 3k rpm.

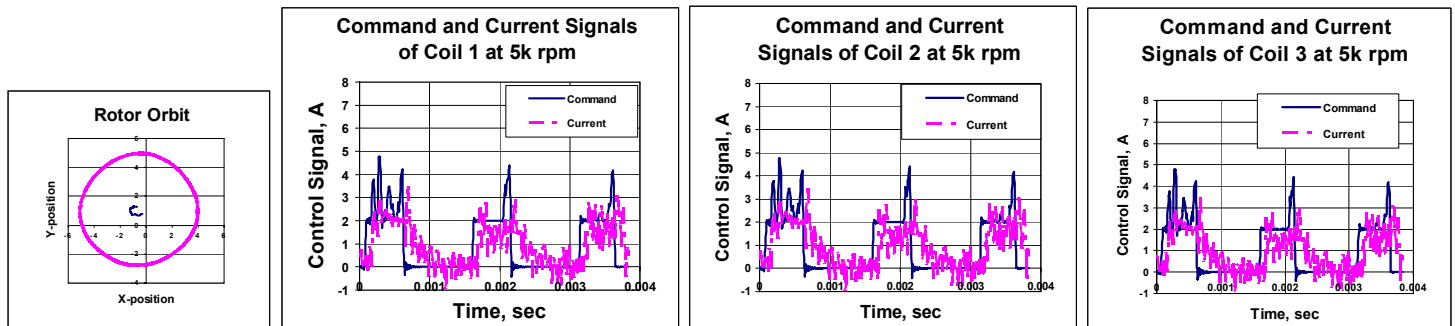


Figure 16.—Rotor orbit within backup bearing clearance circle and command and actual current signals at 5k rpm.

5. Conclusion

A model-based controller using a modified Takemoto's method (added some corrections based on some three-dimensional FEM results) was successfully implemented and demonstrated on the NASA high-power-density SRM, which does not have separate coils for motor action and magnetic bearing action, but only motor coils as in a conventional motor configuration. This feature is an important factor for developing a high specific power motor because it improves power output by having more space for motor windings. Also, our simple observation-based PD controller was developed to avoid mathematical complexity and thereby provide faster real-time calculation at much higher rotor speed. Both controllers were investigated up to the maximum allowable speed of 6500 rpm to determine the optimal controller for our rig. Both controllers worked well in terms of rotor orbit and control current level throughout the speed range.

In this paper, the current preparatory results are confined to the linear range of the magnetic core and to room temperature operation. In the near future, we will extend the self-levitation well into the fully saturated magnetic region where a super high-power-density motor operates. In addition, experimental characterization of magnetic bearing force will be presented in terms of motor current (bias current), negative stiffness, control current, and current stiffness. The bearing load capacity will be compared with theoretical calculation and experimental power measurements will also be presented.

References

1. Brown, G.V., and Siebert, M., "Switched-Reluctance Cryogenic Motor," Research and Technology, NASA/TM—2005-213419, 2005, p. 138.
2. Takemoto, M., Shimada, K., Chiba, A., and Fukao, T., "A Design and Characteristic of Switched Reluctance Type Bearingless Motors," *Proc. 4th Int. Symp. Magnetic Suspension Technology*, NASA/CP—1998-207654, 1998, pp. 49–63.
3. Shuang, Y., Zhiquan, D., and Yangguang, Y., "New Formulae Based on Fourier Extension for Bearingless Switched Reluctance Motors," *Proc. 8th Int. Symp. On Magnetic Bearings*, Mito, Japan, 2002, pp. 53–58.
4. Brown, G.V., Kascak, A., Ebihara, B., Johnson, D., Choi, B., Siebert, M., and Buccieri, C., "NASA Glenn Research Center Program in High Power Density Motors for Aeropropulsion," NASA/TM—2005-13800 (ARL-MR-0628), 2005.
5. Oashima, M., Chiba, A., Fukao, T., and Rahman, M., "Design and Analysis of Permanent Magnet-Type Bearingless Motors," *IEEE Trans. Indus. Electr.*, vol. IE-43, no. 2, 1996, pp. 292–299.
6. Ohishi, T., Okada, Y., and Miyamoto, S., "Levitation Control of IPM Type Rotating Motor," *Fifth International Symposium on Magnetic Bearings*, Kanazawa, 1996, pp. 327–332.
7. Chiba, A., Furuichi, R., Aikawa, Y., Shimada, K., Takamoto, Y., and Fukao, T., "A Stable Operation of Induction Type Bearingless Motors Under Loaded Conditions," *IEEE Trans. Ind. App.* vol. 33, no. 44, 1997, pp. 919–924.
8. Schob, R., "Applications of the Lateral-Force-Motor (LFM)," IPEC-Yokohama'95, 1995, pp. 358–363.
9. Ichikawa, O., Michioka, C., Chiba, A., and Fukao, T., "A Decoupling Control Method of Radial Rotor Positions in Synchronous Reluctance Type Bearingless Motors," IPEC-Yokohama'95, 1995, pp. 346–351.
10. Takemoto, M., Chiba, A., and Fukao, T., "A Method of Determining Advanced Angle of Square-Wave Currents in Bearingless Switched Reluctance Motors," *IEEE Trans. Ind. App.*, vol. 37, no. 6, 2001, pp. 1702–1709.
11. Higuchi, T., Kawakatsu, H., and Iwasawa, T., "A Study on Magnetic Suspension of Switched Reluctance Motor," *IEEE of Japan, Annual Meeting Record 684*, 1989, pp. (6–122)—(6–123).
12. Preston, M., Lyons, J., Richter, E., and Chung, K., "Integrated Magnetic Bearing/Switched Reluctance Machine," U.S. Patent 5,424,595, 1994.
13. Takemoto, M., Chiba, A., and Fukao, T., "A New Control Method of Bearingless Switched Reluctance Motors Using Square-Wave Currents," *IEEE IAS Conf.*, 0-7803-5935-6, 2000, pp. 375–380.
14. Takemoto, M., Suzuki, H., Chiba, A., Fukao, T., and Rahman, M., "Improved Analysis of a Bearingless Switched Reluctance Motor," *IEEE Trans. Ind. App.*, vol. 37, no. 1, 2001, pp. 26–34.

REPORT DOCUMENTATION PAGE			Form Approved OMB No. 0704-0188	
Public reporting burden for this collection of information is estimated to average 1 hour per response, including the time for reviewing instructions, searching existing data sources, gathering and maintaining the data needed, and completing and reviewing the collection of information. Send comments regarding this burden estimate or any other aspect of this collection of information, including suggestions for reducing this burden, to Washington Headquarters Services, Directorate for Information Operations and Reports, 1215 Jefferson Davis Highway, Suite 1204, Arlington, VA 22202-4302, and to the Office of Management and Budget, Paperwork Reduction Project (0704-0188), Washington, DC 20503.				
1. AGENCY USE ONLY (Leave blank)		2. REPORT DATE December 2006		3. REPORT TYPE AND DATES COVERED Technical Memorandum
4. TITLE AND SUBTITLE A Bearingless Switched-Reluctance Motor for High Specific Power Applications			5. FUNDING NUMBERS WBS 561581.02.08.03.06.04	
6. AUTHOR(S) Benjamin B. Choi and Mark Siebert				
7. PERFORMING ORGANIZATION NAME(S) AND ADDRESS(ES) National Aeronautics and Space Administration John H. Glenn Research Center at Lewis Field Cleveland, Ohio 44135-3191			8. PERFORMING ORGANIZATION REPORT NUMBER E-15743	
9. SPONSORING/MONITORING AGENCY NAME(S) AND ADDRESS(ES) National Aeronautics and Space Administration Washington, DC 20546-0001			10. SPONSORING/MONITORING AGENCY REPORT NUMBER NASA TM-2006-214486	
11. SUPPLEMENTARY NOTES Prepared for the 42nd Joint Propulsion Conference and Exhibit cosponsored by the AIAA, ASME, SAE, and ASEE, Sacramento, California, July 9-12, 2006. Benjamin B. Choi, NASA Glenn Research Center; and Mark Siebert, University of Toledo, 2801 W. Bancroft Street, Toledo, Ohio 43606. Responsible person, Benjamin B. Choi, organization code RXS, 216-433-6040.				
12a. DISTRIBUTION/AVAILABILITY STATEMENT Unclassified - Unlimited Subject Category: 07 Available electronically at http://gltrs.grc.nasa.gov This publication is available from the NASA Center for AeroSpace Information, 301-621-0390.			12b. DISTRIBUTION CODE	
13. ABSTRACT (Maximum 200 words) A 12-8 switched-reluctance motor (SRM) is studied in bearingless (or self-levitated) operation with coil currents limited to the linear region to avoid magnetic saturation. The required motoring and levitating currents are summed and go into a single motor coil per pole to obtain the highest power output of the motor by having more space for motor coil winding. Two controllers are investigated for the bearingless SRM operation. First, a model-based controller using the radial force, which is adjusted by a factor derived from finite element analysis, is presented. Then a simple and practical observation-based controller using a PD (proportional-derivative) control algorithm is presented. Both controllers were experimentally demonstrated to 6500 rpm. This paper reports the initial efforts toward eventual self levitation of a SRM operating into strong magnetic core saturation at liquid nitrogen temperature.				
14. SUBJECT TERMS Electric motors; Bearingless rotors; Magnetic bearings; Automatic feedback control			15. NUMBER OF PAGES 20	
			16. PRICE CODE	
17. SECURITY CLASSIFICATION OF REPORT Unclassified	18. SECURITY CLASSIFICATION OF THIS PAGE Unclassified	19. SECURITY CLASSIFICATION OF ABSTRACT Unclassified	20. LIMITATION OF ABSTRACT	

